

# You Only Need One Color Space: An Efficient Network for Low-light Image Enhancement

Qingsen Yan\*, Yixu Feng\*, Cheng Zhang\*, Pei Wang, Peng Wu, Wei Dong, Jinqiu Sun, Yanning Zhang

**Abstract**—Low-Light Image Enhancement (LLIE) task tends to restore the details and visual information from corrupted low-light images. Most existing methods learn the mapping function between low/normal-light images by deep neural networks on sRGB and HSV color space. However, these methods involve sensitivity and instability in the enhancement process, which often generate obvious color and brightness artifacts. To alleviate this problem, we propose a novel trainable color space, named Horizontal/Vertical-Intensity (HVI), which not only decouples brightness and color from RGB channels to mitigate the instability during enhancement, but also adapts to low-light images in different illumination ranges due to the trainable parameters. Furthermore, we design a novel Color and Intensity Decoupling Network (CIDNet) with two branches dedicated to processing the decoupled image brightness and color in the HVI space. In addition, we introduce the Lighten Cross-Attention (LCA) module to facilitate interaction between image structure and content information in both branches, while also suppressing noise in low-light images. We conduct 22 quantitative and qualitative experiments to show that the proposed CIDNet outperforms the state-of-the-art methods on 11 datasets. The code is available at <https://github.com/Fediory/HVI-CIDNet>.

**Index Terms**—Low-Light Image Enhancement, HVI Color Space, Transformer, Supervised Learning.

## I. INTRODUCTION

Under low-light conditions, the sensor captures weak light signals with severe noise, resulting in poor visual quality for low-light images. Obtaining high-quality images from degraded images often necessitates Low-Light Image Enhancement (LLIE), intending to improve the brightness while simultaneously reducing the impact of noise and color bias [1].

The majority of existing LLIE approaches [2]–[4] focus on finding an appropriate image brightness, and commonly employ deep neural networks to learn the mapping relationship between low-light images and normal-light images within the sRGB space. However, image brightness and color exhibit a strong interdependence with the three channels in sRGB. A slight disturbance in the color space will cause an obvious variation in both the brightness and color of the generated image. As illustrated in Fig. 1, introducing noise to one dimension (red channel) in the sRGB space dramatically changes the color of the enhanced image. This suggests a mismatch between sRGB space and the low-light enhancement

Q. Yan, Y. Feng, C. Zhang, P. Wang, P. Wu, J. Sun and Y. Zhang are with the School of Computer Science, Northwestern Polytechnical University.

W. Dong is with the School of Computer Science, Xi'an University of Architecture and Technology.

\*These authors contributed equally to this work. Corresponding author: Yanning Zhang

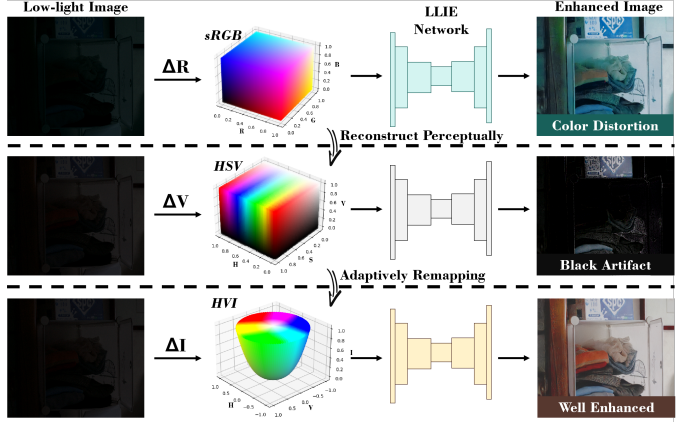


Fig. 1: The sensitivity comparison of different color spaces in low-light enhancement. The notations  $\Delta R$ ,  $\Delta V$ , and  $\Delta I$  represent a tiny variation in the axis of Red (sRGB), Value (HSV), and Intensity (HVI), respectively. After enhancement processing, noticeable color artifacts can be observed in the sRGB and HSV space results.

processing, resulting in instability in both brightness and color in the enhanced results. The inherent instability leads to the existing enhancement methods [3], [5] requiring more parameters and complex network architecture to learn this enhancement mapping. It is also why numerous low-light enhancement methods [6], [7] need to incorporate additional brightness and color losses during training.

While the HSV color space [8] enables the separation of brightness and color of the image from sRGB channels, the discontinuous property of hue axis (see Sec. III-B) and its intricate mapping relationships with sRGB space makes it challenging to handle complex and varying lighting conditions. As shown in Fig. 1, enhanced images with the HSV space often have obvious black artifacts due to extremely low light environments. We consider that the color space (e.g., sRGB, HSV) has a huge impact on the image enhancement effect.

To address the aforementioned issue between the low-light image enhancement task and existing color spaces, we introduce a new color space named **Horizontal/Vertical-Intensity (HVI)**, designed specifically to cater to the needs of low-light enhancement tasks. The proposed HVI color space not only decouples brightness and color information but also incorporates three trainable representation parameters and a trainable function, allowing it to adapt to the brightening scale and color variations of different low-light images. Building upon the HVI color space, to fully leverage the decoupled information, we propose a new LLIE method, named **Color and Intensity Decoupling Network (CIDNet)**. CIDNet consists

of HV-branch and intensity-branch, which makes full use of decoupled information to generate high-quality results. After applying the HVI transformation to the image, it is separately fed into the HV-branch to extract color information, and the intensity-branch to establish the photometric mapping function under different lighting conditions. Additionally, to enhance the interaction between the structures of images contained in the brightness and color branches, we propose the bidirectional Lighten Cross-Attention (LCA) module to learn the complementary information of HV-branch and intensity-branch. Furthermore, we conduct experiments and ablation studies on multiple datasets to validate our approach. The experimental results demonstrate that CIDNet effectively enhances the brightness of low-light images while preserving their natural colors, which validates the compatibility of the proposed HVI color space with low-light image enhancement tasks. Note that the proposed method exhibits relatively small parameters (1.88M) and computational loads (7.57G), achieving a good balance between effectiveness and efficiency on edge devices.

Our contributions can be summarized as follows:

- 1) We introduce a novel HVI color space with trainable parameters, which not only decouples the image brightness and color, but also adapts to various image illumination scales.
- 2) Based on the HVI color space, we propose a dual-branch network, CIDNet, to concurrently process the brightness and color of low-light images.
- 3) We design a LCA module to facilitate interaction between the HV-branch and intensity-branch, allowing the scene information in each branch to complement and improve the visual effects of the enhanced image.
- 4) We conduct 22 quantitative and qualitative experiments that our CIDNet outperforms all types of SOTA methods on 10 different metrics across 11 datasets.

## II. RELATED WORK

### A. Low-Light Image Enhancement

**Traditional and Plain LLIE Methods.** Plain methods usually enhanced image by histogram equalization [9] and Gama Correction [10]. Traditional method [11] commonly depends on the application of the Retinex theory, which decomposes the lights into illumination and reflections. For example, Guo *et al.* [12] refine the initial illumination map to optimize lighting details by imposing a structure prior. Regrettably, existing methodologies are inadequate in effectively eliminating noise artifacts and producing accurate color mappings, rendering them incapable of achieving the desired level of precision and finesse in the LLIE tasks.

**Deep Learning Methods.** Deep learning-based approaches [2], [3], [13], [14] has been widely used in LLIE task. Existing methods propose distinct solutions to address the issues of image color shift and noise stabilization. For instance, RetinexNet [6] enhances images by decoupling illumination and reflectance based on Retinex theory. However, it has unsatisfied results with several color shifts. SNR-Aware [15] presents a collectively exploiting Signal-to-Noise-Ratio-aware transformers to dynamically enhance pixels with spatial-varying operations, which could reduce the color bias and

noise. Bread [8] decouples the entanglement of noise and color distortion by using YCbCr color space. Furthermore, they designed a color adaption network to tackle the color distortion issue left in light-enhanced images. Still, SNR-Aware and Bread show poor generalization ability. They are not only inaccurately controlled in terms of brightness in some of the datasets, but also biased in terms of color with pure black area.

**Diffusion Model-based Methods.** With the advancement of Denoising Diffusion Probabilistic Models (DDPMs) [16], diffusion-based generative models have achieved remarkable results in the LLIE task. It has indeed shown the capability to generate more accurate and appropriate images in pure black spaces devoid of information and under low light conditions with significant noise. However, they still exhibit issues such as local overexposure or color shift. Recent LLIE diffusion methods have attempted to address these challenges by incorporating global supervised brightness correction or employing local color correctors [17]–[19]. PyDiff [17] employs a Global Feature Modulation to correct the pixel noise and color bias globally. Diff-Retinex [20] rethink the retinex theory with a diffusion-based model in the LLIE task, which decomposed an image to illumination and reflectance colors to reduce color bias and enhance brightness separately. However, the aforementioned diffusion models suffer from long training and inference times, lack of Lighten efficiency, and inability to fully decouple brightness and color information.

### B. Color Space

**RGB.** Currently, the most commonly used is the standard-RGB (sRGB) color space. For the same principle as visual recognition by the human eye, sRGB is widely used in digital imaging devices [21]. Nevertheless, image brightness and color exhibit a strong interdependence with the three channels in sRGB. A slight disturbance in the color space will cause an obvious variation in both the brightness and color of the generated image. Thus, sRGB is not the optimal color space for enhancement.

**HSV and YCbCr.** Hue, Saturation and Value (HSV) color space represents points in an RGB color model with a cylindrical coordinate system [22]. Indeed, it does decouple brightness and color of the image from RGB channels. However, the inherent hue axis color discontinuity and non-mono-mapped pure black planes pose significant challenges when attempting to enhance the image in HSV color space, resulting in the emergence of obvious artifacts. To circumvent issues related to HSV, some methods [8], [23] also transform sRGB images to the YCbCr color space for processing, which has an illumination axis (Y) and reflect-color-plain (CbCr). Although it solved the hue dimension discontinuity problem of HSV, the multi-mapping of pure black planes still exists.

## III. HVI COLOR SPACE

To address the misalignment between LLIE and existing color spaces, we innovatively introduce a trainable color space in the field of LLIE, named Horizontal/Vertical-Intensity (HVI) color space. HVI color space consists of three trainable

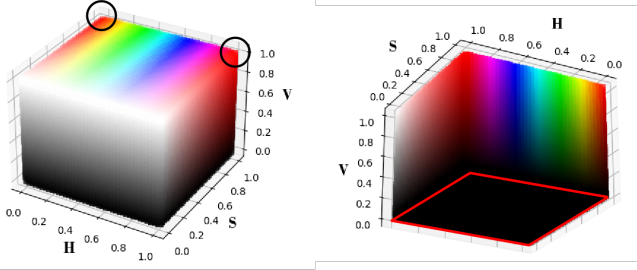


Fig. 2: HSV color space visualization. The two black circles in the left image indicate the discontinuous color positions along the hue axis, while the red box in the right image displays a pure black plane with Value= 0.

parameters and a custom training function that can adapt to the photosensitive characteristics and color sensitivities of low-light images. In this section, we will present the description of the mono-mapping image transformation from sRGB space to HVI color space, as well as the details of HVI color space.

### A. Intensity Map

In the task of LLIE, one crucial aspect is accurately estimating the illumination intensity map of the scene. Following retinex-based LLIE methods [6], [7], [12], we represent the intensity map of an image with the maximum value among the RGB channels. According to the definition, we can calculate the intensity map of an image  $\mathbf{I}_{max} \in \mathbb{R}^{H \times W \times 3}$  as follows:

$$\mathbf{I}_{max} = \max_{c \in \{R, G, B\}} (\mathbf{I}_c), \quad (1)$$

Next, we will introduce how to utilize the intensity map to guide the generation of the corresponding HV color map.

### B. HV Transformation

To effectively address color deviations, previous LLIE methods typically separate an sRGB image into a reflectance map [2], [6] based on the retinex theory. These approaches often require a large computational network for fitting, which need to use a combination of hue and saturation to simulate the reflectance map. However, the HSV color space is discontinued in the hue axis (see the black circles in Fig. 2) and has a non-bijection pure black plane (see the red rectangle in Fig. 2), which disrupts the one-to-one mapping. For discontinuity of the hue axis, based on HSV color transform formula, a red color in sRGB  $(R, G, B) = (1, 0, 0)$  corresponds to  $(0, 1, 1)$  and  $(1, 1, 1)$  in HSV color space. For the pure black plane, as shown in Fig. 2, any HSV pixel with Value= 0 denote the black color, corresponding to  $(R, G, B) = (0, 0, 0)$  in sRGB color space. Thus, the one-to-many mapping is the source reason of why the existing methods on HSV color space generate the obvious artifacts in the dark regions.

To address the suboptimum problems caused by one-to-many mapping (HSV color space), we design a trainable Horizontal/Vertical (HV) color map as a plane to quantify a color-reflectance map, which is a one-to-one mapping to sRGB color space. The HVI color space consists of three trainable parameters  $k$ ,  $\gamma_G$  and  $\gamma_B$ , and a custom training function  $T(x)$ .

**Parameter  $k$ .** Considering that the dark regions of low-light images have small values, which is hard to distinguish the color and causes information loss. Based on the proposed HVI color space, we customize a parameter  $k$  that allows networks to adjust the color point density of the low-intensity color plane, which quantifies a Color-Density- $k$  ( $\mathbf{C}_k$ ) as

$$\mathbf{C}_k = \sqrt[k]{\sin\left(\frac{\pi \mathbf{I}_{max}}{2}\right) + \varepsilon}, \quad (2)$$

where  $k \in \mathbb{Q}^+$  and we set  $\varepsilon = 1 \times 10^{-8}$ .

**Hue bias parameter  $\gamma_G$  and  $\gamma_B$ .** Since different cameras have different sensitivity on RGB channel, it will cause color shift (*i.e.* green color) on the low-light scenes. To alleviate the data diversity caused by color shift, we learn an adaptive linear Color-Perceptual map  $\mathbf{P}_\gamma$  on hue value.

$$\mathbf{P}_\gamma = \begin{cases} 3\gamma_G \mathbf{H}, & \text{if } 0 \leq \mathbf{H} < \frac{1}{3} \\ 3(\gamma_B - \gamma_G)(\mathbf{H} - \frac{1}{3}) + \gamma_G, & \text{if } \frac{1}{3} \leq \mathbf{H} < \frac{2}{3} \\ 3(1 - \gamma_B)(\mathbf{H} - 1) + 1, & \text{if } \frac{2}{3} \leq \mathbf{H} \leq 1 \end{cases}, \quad (3)$$

where  $\gamma_G, \gamma_B \in (0, 1)$ ,  $\mathbf{H} \in [0, 1]$  denotes the hue value.

**Customizable or trainable function  $T(x)$ .** To improve the saturation the generated results, we design a Function-Density- $T$  based on the  $\mathbf{P}_\gamma$  to adaptively adjust the saturation. We utilize a Function-Density- $T$  as

$$\mathbf{D}_T = T(\mathbf{P}_\gamma), \quad (4)$$

where  $T(\cdot)$  satisfies  $T(0) = T(1)$  and  $T(\mathbf{P}_\gamma) \geq 0$ . Finally, we formalize the horizontal ( $\hat{\mathbf{H}}$ ) and vertical ( $\hat{\mathbf{V}}$ ) plane as

$$\begin{aligned} \hat{\mathbf{H}} &= \mathbf{C}_k \odot \mathbf{S} \odot \mathbf{D}_T \odot h, \\ \hat{\mathbf{V}} &= \mathbf{C}_k \odot \mathbf{S} \odot \mathbf{D}_T \odot v, \end{aligned} \quad (5)$$

where  $\odot$  denotes the element-wise multiplication. Note that we orthogonalize our color map by setting an intermediate variable  $h = \cos(2\pi \mathbf{P}_\gamma)$  and  $v = \sin(2\pi \mathbf{P}_\gamma)$  to be bijective.

### C. Perceptual-invert HVI Transformation

To convert HVI back to the HSV color space, we design a Perceptual-invert HVI Transformation (PHVIT), which is a surjective mapping while allowing for the independent adjustment of the image's saturation and brightness.

To transform injectively, the PHVIT sets  $\hat{h}$  and  $\hat{v}$  as an intermediate variable as

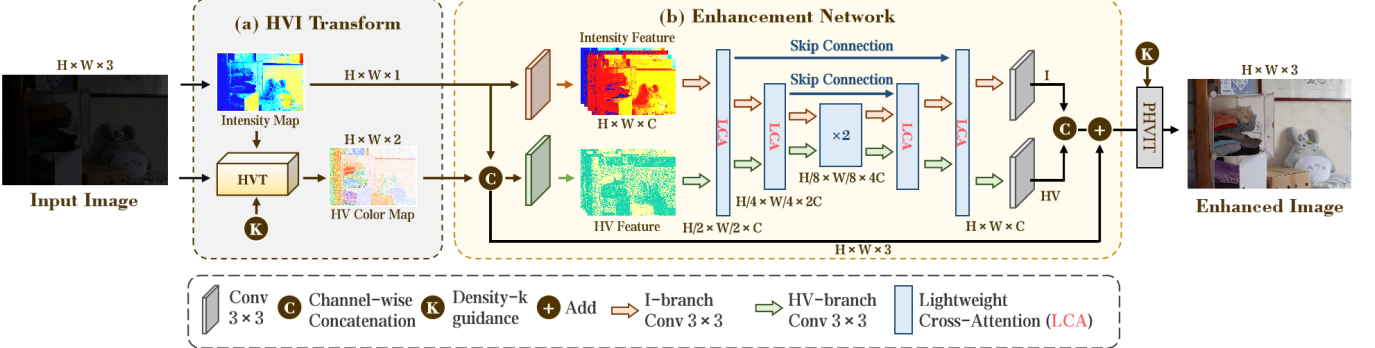
$$\hat{h} = \frac{\hat{\mathbf{I}}_{\mathbf{H}}}{\mathbf{D}_T \mathbf{C}_k + \varepsilon}, \hat{v} = \frac{\hat{\mathbf{I}}_{\mathbf{V}}}{\mathbf{D}_T \mathbf{C}_k + \varepsilon}, \quad (6)$$

where  $\varepsilon = 1 \times 10^{-8}$ . Then, we convert  $\hat{h}$  and  $\hat{v}$  to HSV color space. The hue map can be formulated by

$$H = F_\gamma(\arctan(\frac{\hat{v}}{\hat{h}}) \bmod 1), \quad (7)$$

where  $F_\gamma$  is a inverse linear function as

$$F_\gamma(\mathbf{X}) = \begin{cases} \frac{\mathbf{X}}{3\gamma_G}, & \text{if } 0 \leq \mathbf{X} < \gamma_G \\ \frac{\mathbf{X} - \gamma_G}{3(\gamma_B - \gamma_G)} + \frac{1}{3}, & \gamma_G \leq \mathbf{X} < \gamma_B \\ \frac{\mathbf{X} - 1}{3(1 - \gamma_B)} + 1, & \gamma_B \leq \mathbf{X} \leq 1 \end{cases}, \quad (8)$$



where  $\gamma_G, \gamma_B$  are mentioned in Eq. 3. The saturation and value map can be perceptually estimated as

$$S = \alpha_S \sqrt{\hat{h}^2 + \hat{v}^2}, \quad (9)$$

$$V = \alpha_I \hat{\mathbf{I}}_I,$$

where  $\alpha_s, \alpha_i$  are the customizing linear parameters to change the image color saturation and brightness. Finally, we will obtain the sRGB image with HSV image [22].

#### IV. CIDNET

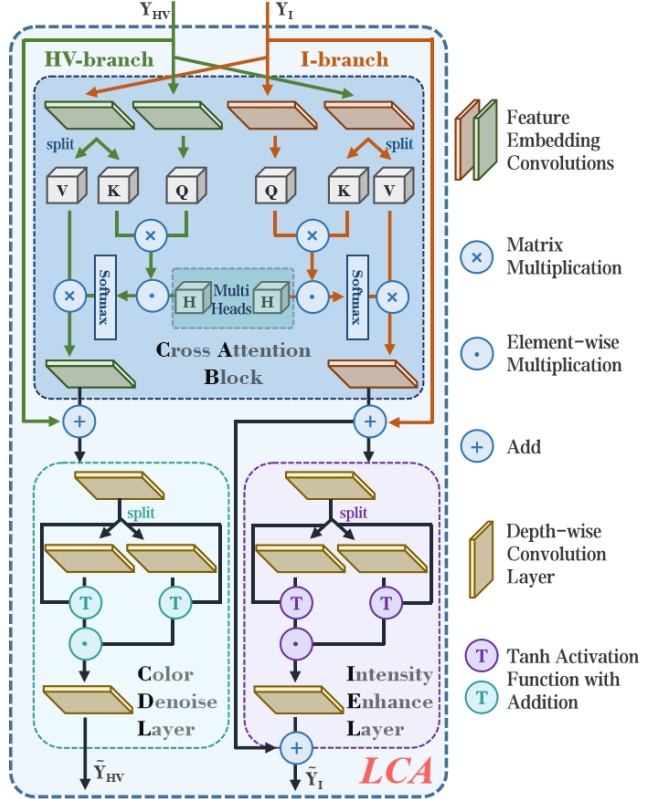
Based on the proposed HVI space, we introduce a novel dual-branch LLIE network, named the Color and Intensity Decoupling Network (CIDNet) to separately address HV-plain and I-axis information in the HVI space. The CIDNet employs HV-branch to suppress the noise and chromaticity in the dark regions and utilizes I-branch to estimate the luminance of the whole images. Furthermore, we design an Lighten Cross-Attention (LCA) module to facilitate interaction guidance between the HV-branch and I-branch. In this section, we provide a detailed description of the architecture of CIDNet.

##### A. Pipeline

As shown in Fig. 3, the overall framework can be divided into three consecutive main steps, *i.e.*, HVI transformation, enhancement network, and perceptual-inverse HVI transformation.

As described in Sec. III, the HVI transformation decomposes the sRGB image into two components: an intensity map containing scene illuminance information and an HV color map containing scene color and structure information. Specifically, we first calculate the intensity map using Eq. 1, which is  $\mathbf{I}_I = \mathbf{I}_{max}$ . Subsequently, we utilize the intensity map and the original image to generate HV color map using Eq. 5. Furthermore, a trainable density- $k$  is employed to adjust the color point density of the low-intensity color plane, as shown in Fig. 3(a).

Based on the UNet architecture, the enhancement network takes an intensity map and HV color map as input. To learn the initial information of intensity map and HV color map, we employ  $3 \times 3$  convolutional layers to obtain the features with



same dimension in each branch. Subsequently, the features are fed into the UNet with Lighten Cross-Attention (LCA) modules. The LCA module consists of cross attention blocks, color denoise layer and intensity enhance layer. The cross attention block learns the corresponding interacted information between the HV-branch and I-branch. The color denoise layer avoids noise artifacts and color shift, and the intensity enhance layer improves the luminance and removes the saturated regions. The final outputs of UNet are the refined intensity and HV

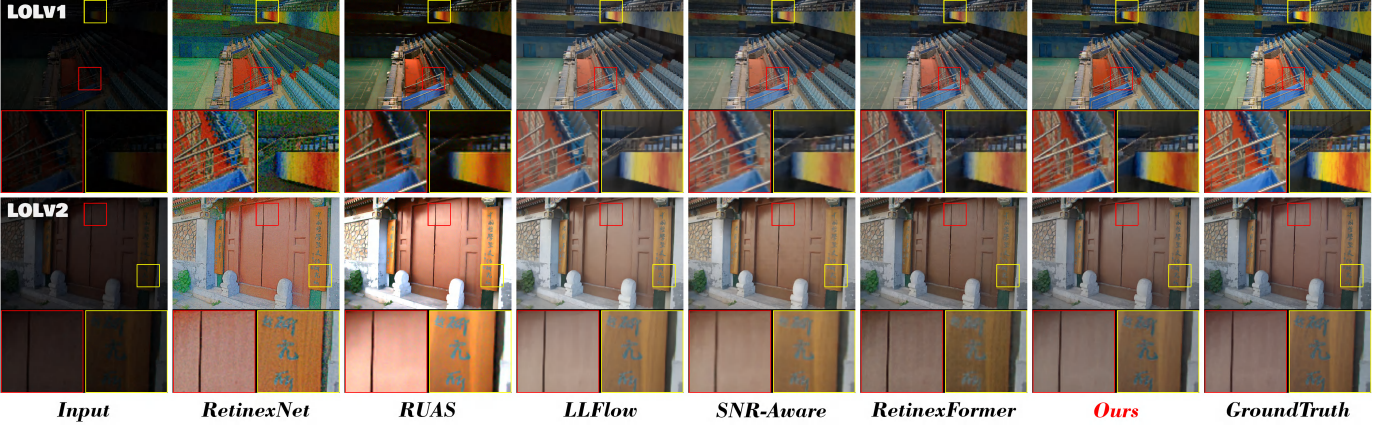


Fig. 5: Visual comparisons of the enhanced results by different methods on LOLv1 and LOLv2. (Zoom in for the best view.)

maps. To decrease the difficulty of the learning process, we employ a residual mechanism to add the original HVI map. Finally, we perform an HVI inverse transformation with the trainable parameter density- $k$  to map the image to the sRGB space.

### B. Structure

1) *Enhancement Network*: As depicted in Fig. 3(b), we use the commonly employed UNet as the baseline network, which has an encoder, decoder, and multiple skip connections. The encoder includes three LCA blocks and downsample and  $3 \times 3$  kernel convolutional layers. Similarly, the decoder consists of three LCA modules, and upsampling layers.

2) *Lighten Cross-Attention*: To enhance the interaction between the structures of images contained in the brightness and color branches, we propose the Lighten Cross-Attention (LCA) module to learn the complementary information of HV-branch and intensity-branch. As shown in Fig. 4, the HV-branch and I-branch in LCA handle HV features and intensity features, respectively. To learn the complementary potential between HV features and intensity features during the processing, we propose cross attention block (**CAB**) to facilitate mutual guidance between HV features and intensity features. To force the CAB to learn the information from the opposite branch (*i.e.*, HV branch only use the information of I-branch to refine itself), we utilize the one branch as the query and leverage another branch as key and value in the CAB.

As shown in 4, The CAB exhibits a symmetrical structure between the I-way and HV-way. We use the I-branch as an example to describe the details.  $\mathbf{Y}_I \in \mathbb{R}^{\hat{H} \times \hat{W} \times \hat{C}}$  denotes the inputs of I-branch, our CAB first derives query ( $\mathbf{Q}$ ) by  $\mathbf{Q} = W^{(Q)}\mathbf{Y}_I$ . Meanwhile, the CAB splits key ( $\mathbf{K}$ ) and value ( $\mathbf{V}$ ) by  $\mathbf{K} = W^{(K)}\mathbf{Y}_I$  and  $\mathbf{V} = W^{(V)}\mathbf{Y}_I$ .  $W^{(Q)}$ ,  $W^{(K)}$  and  $W^{(V)}$  represents the feature embedding convolution layers. We formulate as

$$\hat{\mathbf{Y}}_I = W(\mathbf{V} \otimes \text{Softmax}(\mathbf{Q} \otimes \mathbf{K}/\alpha_H) + \mathbf{Y}_I) \quad (10)$$

where  $\alpha_H$  is the multi-head factor [24] and  $W(\cdot)$  denotes the feature embedding convolutions.

Next, following Retinex theory, intensity enhance layer (IEL) decomposes the tensor  $\hat{\mathbf{Y}}_I$  as  $\mathbf{Y}_I = W^{(I)}\hat{\mathbf{Y}}_I$  and  $\mathbf{Y}_R = W^{(R)}\hat{\mathbf{Y}}_I$ . The IEL is defined as

$$\begin{aligned} \tilde{\mathbf{Y}}_I &= W_s((\tanh(W_s\mathbf{Y}_I) + \mathbf{Y}_I) \\ &\quad \odot (\tanh(W_s\mathbf{Y}_R) + \mathbf{Y}_R)) \end{aligned} \quad (11)$$

where  $\odot$  represents the element-wise multiplication and  $W_s$  denotes the depth-wise convolution layers. Finally, the output of IEL adds the residuals to simplify the training process.

### C. Loss Function

To integrate the advantages of HVI space and the sRGB space, the loss function consists both color spaces. In HVI color space, we utilize L1 loss  $L_1$ , edge loss  $L_e$  [25], and perceptual loss  $L_p$  [26] for the low-light enhancement task. It can be expressed as

$$\begin{aligned} l(\hat{X}_{HVI}, X_{HVI}) &= \lambda_1 \cdot L_1(\hat{X}_{HVI}, X_{HVI}) \\ &\quad + \lambda_e \cdot L_e(\hat{X}_{HVI}, X_{HVI}), \\ &\quad + \lambda_p \cdot L_p(\hat{X}_{HVI}, X_{HVI}) \end{aligned} \quad (12)$$

where  $\lambda_1, \lambda_e, \lambda_p$  are all the weight to trade-off the loss function  $l(\cdot)$ . In sRGB color space, we employ the same loss function as  $l(\hat{I}, I)$ . Therefore, our overall loss function  $L$  is represented by

$$L = \lambda_c \cdot l(\hat{\mathbf{I}}_{HVI}, \mathbf{I}_{HVI}) + l(\hat{\mathbf{I}}, \mathbf{I}) \quad (13)$$

where  $\lambda_c$  is the weight to balance the loss in different color spaces.

## V. EXPERIMENTS

### A. Datasets and Settings

We employ seven commonly-used LLIE benchmark datasets for evaluation, including LOLv1 [6], LOLv2 [27], DICM [28], LIME [12], MEF [29], NPE [30], and VV [31]. We also conduct further experiments on two extreme datasets, SICE [32] (containing mix and grad test sets [33]) and SID (Sony-Total-Dark) [34]. Since blurring is often prone to occur in low-luminosity images, to demonstrate the robustness of our CIDNet to multitasking, we conducted experiments on LOL-Blur [35] as well.

TABLE I: Quantitative comparisons PSNR/SSIM↑ on LOL (v1 and v2) datasets. Normal and GT Mean represent with and without gamma-corrected by GroundTruth. The highest result is in red color, the second highest result is in cyan color, and the third is in green. wP and oP represent to train on CIDNet with and without perceptual loss [36].

Methods	Complexity		LOLv1				LOLv2-Real				LOLv2-Syn			
			Normal		GT Mean		Normal		GT Mean		Normal		GT Mean	
	Params/M	FLOPs/G	PSNR	SSIM										
RetinexNet [6]	0.84	584.47	16.774	0.419	18.915	0.427	16.097	0.401	18.323	0.447	17.137	0.762	19.099	0.774
Kind [2]	8.02	34.99	17.650	0.775	20.860	0.802	14.740	0.641	17.544	0.669	13.290	0.578	16.259	0.591
ZeroDCE [4]	0.075	4.83	14.861	0.559	21.880	0.640	16.059	0.580	19.771	0.671	17.712	0.815	21.463	0.848
3DLUT [37]	0.59	7.67	14.350	0.445	21.350	0.585	17.590	0.721	20.190	0.745	18.040	0.800	22.173	0.854
DRBN [38]	5.47	48.61	16.290	0.617	19.550	0.746	20.290	0.831	-	-	23.220	0.927	-	-
RUAS [39]	0.003	0.83	16.405	0.500	18.654	0.518	15.326	0.488	19.061	0.510	13.765	0.638	16.584	0.719
LLFlow [5]	17.42	358.4	21.149	0.854	24.998	0.871	17.433	0.831	25.421	0.877	24.807	0.919	27.961	0.930
EnlightenGAN [3]	114.35	61.01	17.480	0.651	20.003	0.691	18.230	0.617	-	-	16.570	0.734	-	-
Restormer [40]	26.13	144.25	22.365	0.816	26.682	0.853	18.693	0.834	26.116	0.853	21.413	0.830	25.428	0.859
LEDNet [35]	7.07	35.92	20.627	0.823	25.470	0.846	19.938	0.827	27.814	0.870	23.709	0.914	27.367	0.928
SNR-Aware [15]	4.01	26.35	24.610	0.842	26.716	0.851	21.480	0.849	27.209	0.871	24.140	0.928	27.787	0.941
PairLIE [7]	0.33	20.81	19.510	0.736	23.526	0.755	19.885	0.778	24.025	0.803	-	-	-	-
LLFormer [41]	24.55	22.52	23.649	0.816	25.758	0.823	20.056	0.792	26.197	0.819	24.038	0.909	28.006	0.927
RetinexFormer [14]	1.53	15.85	25.153	0.846	27.140	0.850	22.794	0.840	27.694	0.856	25.670	0.930	28.992	0.939
<b>CIDNet-wP</b>	1.88	7.57	<b>23.809</b>	<b>0.857</b>	<b>27.715</b>	<b>0.876</b>	<b>24.111</b>	<b>0.868</b>	<b>28.134</b>	<b>0.892</b>	<b>25.129</b>	<b>0.939</b>	<b>29.367</b>	<b>0.950</b>
<b>CIDNet-oP</b>	1.88	7.57	23.500	0.870	28.141	0.889	23.427	0.862	27.762	0.881	25.705	0.942	29.566	0.950



Fig. 6: Input Sony-Total-Dark extreme low-light image with the image enhanced by our CIDNet.

**LOL.** The LOL dataset has v1 [6] and v2 [27] versions. LOL-v2 is divided into real and synthetic subsets. The training and testing sets are split in proportion to 485:15, 689:100, and 900:100 on LOL-v1, LOL-v2-Real, and LOL-v2-Synthetic. For LOLv1 and LOLv2-Real, we crop the training images into  $400 \times 400$  patches and train CIDNet for 1500 epochs with a batch size of 8. For LOLv2-Synthetic, we set the batch size to 1 and trained 500 epochs without cropping.

**SICE.** The original SICE dataset [32] contains a total of 589 sets of low-light and overexposed images, and the training set, validation set, and test set are divided into three groups according to 7:1:2. We train on the SICE training set with the batch size of 10 and test on the datasets SICE-Mix and SICE-Grad [33]. We crop the original SICE image by  $160 \times 160$  and train CIDNet over 1000 epochs.

**Sony-Total-Dark.** This dataset is a customized version of the subset of SID dataset captured by the Sony  $\alpha$ 7S II camera, which is adopted for evaluation. There are 2697 short-long-exposure RAW image pairs. To make this dataset more challenging, we convert the RAW format images to sRGB

TABLE II: Quantitative comparisons LPIPS/FLOPs↓ on LOL (v1 and v2) datasets. GT Mean represents the gamma-corrected image by GroundTruth. The best result is in red color.

Methods	LOLv1		LOLv2-Real		LOLv2-Syn		Complexity FLOPs/G↓
	Normal	GT Mean	Normal	GT Mean	Normal	GT Mean	
EnlightenGAN	0.322	0.317	0.309	0.301	0.220	0.213	61.01
RetinexNet	0.474	0.470	0.543	0.519	0.255	0.247	587.47
LLFormer	0.175	0.167	0.211	0.209	0.066	0.061	22.52
LLFlow	0.119	0.117	0.176	0.158	0.067	0.063	358.4
LEDNet	0.118	0.113	0.120	0.114	0.061	0.056	35.92
RetinexFormer	0.131	0.129	0.171	0.166	0.059	0.056	15.85
<b>CIDNet</b>	<b>0.086</b>	<b>0.079</b>	<b>0.108</b>	<b>0.101</b>	<b>0.045</b>	<b>0.040</b>	<b>7.57</b>

images with *no gamma correction* as Fig. 6, which resulted in images becoming extremely dark. We crop the training images into  $256 \times 256$  patches and train CIDNet for 1500 epochs with a batch size of 4.

**LOL-Blur.** The dataset, LOL-Blur [35], contains 12,000 low-blur/normal-sharp pairs with diverse darkness and blurs in 200 different scenarios. The training and testing sets are split in proportion to 17:3. In our experiment, we use low-blur and high-sharp-scaled sets for training and testing. We crop the training images into  $256 \times 256$  patches and train CIDNet for 300 epochs with a batch size of 8. Unlike other experiments, here we use  $l_{mse}$  Loss instead of  $l_1$  Loss in Eq. 12.

**Experiment Settings.** We implement our CIDNet by PyTorch. The model is trained with the Adam [42] optimizer ( $\beta_1 = 0.9$  and  $\beta_2 = 0.999$ ) for at least 300 epochs by using a single NIVIDA 2080Ti or 3090 GPU. The learning rate is initially set to  $1 \times 10^{-4}$  and then steadily decreased to  $1 \times 10^{-7}$  by the cosine annealing scheme [43] during the training process. In testing stage, we pad the input images to be a multiplier of  $8 \times 8$  using reflect padding on both sides. After inference, we crop the padded image back to its original size. Since the outliers are existed in the outputs of UNets, we simply use clip operation to HVI space, which follows  $\mathbb{D} = \{p = (h, v, i) \mid h^2 + v^2 \leq \sin^{\frac{2}{k}}(\frac{\pi i}{2})\}, 0 \leq i \leq 1\}$ , where  $p = (h, v, i)$  is the three-dimensional coordinates in HVI color space, and  $k$  denotes the density- $k$  in Eq. 2.

**Evaluation Metrics.** For the *paired* dataset, we adopt the

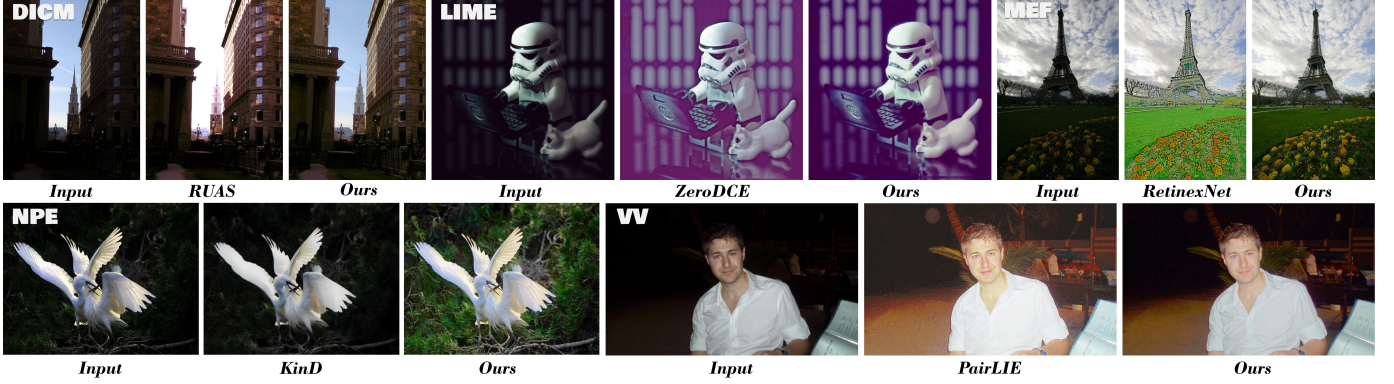


Fig. 7: Five unpaired datasets are compared visually, and we randomly select one image in each dataset to compare with the other methods. Our CIDNet enhances dark details and illumination to a suitable interval, which is better than the other methods.

TABLE III: Quantitative comparison on five unpaired datasets with **BRISQUE**↓ and **NIQE**↓. The best result is in red color.

Methods	DICM		LIME		MEF		NPE		VV	
	BRISQUE↓	NIQE↓								
KinD [2]	48.72	5.15	39.91	5.03	49.94	5.47	36.85	4.98	50.56	4.30
ZeroDCE [4]	27.56	4.58	20.44	5.82	17.32	4.93	20.72	4.53	34.66	4.81
RUAS [39]	38.75	5.21	27.59	4.26	23.68	3.83	47.85	5.53	38.37	4.29
LLFlow [5]	26.36	4.06	27.06	4.59	30.27	4.70	28.86	4.67	31.67	4.04
SNR-Aware [15]	37.35	4.71	39.22	5.74	31.28	4.18	26.65	4.32	78.72	9.87
PairLIE [7]	33.31	4.03	25.23	4.58	27.53	4.06	28.27	4.18	39.13	3.57
<b>CIDNet</b>	<b>21.47</b>	<b>3.79</b>	<b>16.25</b>	<b>4.13</b>	<b>13.77</b>	<b>3.56</b>	<b>18.92</b>	<b>3.74</b>	<b>30.63</b>	<b>3.21</b>

Peak Signal-to-Noise Ratio (PSNR) and Structural Similarity (SSIM) [44] as the distortion metrics. To comprehensively evaluate the perceptual quality of restored images, we report Learned Perceptual Image Patch Similarity (LPIPS) [45] by using AlexNet [46] for references as a perceptual metric. For the *unpaired* datasets, we evaluated single recovered images using BRISQUE [47] and NIQE [48] perceptually.

### B. Evaluation on Image Enhancement

**LOL Datasets Results.** We quantitatively compare our CIDNet with many SOTA methods as shown in Table I and II. It can be found that our method is optimal on almost all metrics for both LOLv1 and LOLv2 datasets. Comparing the two tables comprehensively, it can be seen that CIDNet achieves six new SOTA SSIM and LPIPS results on three subsets of LOL (v1 and v2) dataset with **only 7.57 GFLOPs**. It outperforms the current SOTA method Retinexformer in terms of both PSNR and SSIM under GT Mean while LPIPS improves by **38%**, **39%**, and **29%**, respectively, and FLOPs decreased by **52%**. Compared to 3DLUT with about the same size of FLOPs, our method significantly improves the PSNR

by **6.791**, **7.944**, and **7.393 dB**. It may be observed in Figure 5 that our model restores colors extremely well, which may be attributed to the HVI color space.

**SICE and Sony-total-Dark.** To verify that our model also performs well on large-scale datasets, we conducted experiments on two extremely difficult-to-recover datasets, SICE (including Mix and Grad) and SID-Total-Dark. The three metrics of our CIDNet **are optimal on all three test sets** as Table IV. especially on the Sony-Total-Dark dataset, which outperforms LEDNet by **9.96%** for the PSNR, **4.32%** for the SSIM, **12.74%** for the LPIPS metrics.

**Unpaired Datasets Experiments.** In the case of unpaired datasets DICM, LIME, MEF, NPE, and VV, where GroundTruth is unavailable, we evaluate the effectiveness of models trained on LOLv1 or LOLv2-Syn using various methods, and measure their performance using BRISQUE and NIQE metrics. We report our comparisons against SOTA methods as Table III, where our method outperformed all

TABLE V: Ablation of CIDNet module designs. The first row is a simple UNet baseline [49] without attention module. The row (2), (3), (4), (6), and (7) (where the rows with LCA but without CrossAttn) use Self-Attention [40] to replace Cross-Attention.

	Color Space	LCA	Dual-branch	CrossAttn	PSNR↑	SSIM↑
1	sRGB				16.518	0.721
2	sRGB	✓			18.606	0.822
3	HSV	✓			13.237	0.365
4	HSV	✓	✓		10.236	0.254
5	HSV	✓	✓	✓	13.668	0.407
6	HVI	✓			22.000	0.853
7	HVI	✓	✓		23.159	0.854
8	HVI	✓	✓	✓	<b>24.111</b>	<b>0.868</b>

TABLE IV: Quantitative comparison on three hard datasets (SICE-Mix/Grad and Sony-Total-Dark) with **PSNR↑**, **SSIM↑** and **LPIPS↓**.

Methods	SICE-Mix			SICE-Grad			Sony-Total-Dark		
	PSNR↑	SSIM↑	LPIPS↓	PSNR↑	SSIM↑	LPIPS↓	PSNR↑	SSIM↑	LPIPS↓
RetinexNet	12.397	0.606	0.407	12.450	0.619	0.364	15.695	0.395	0.743
ZeroDCE	12.428	0.633	0.382	12.475	0.644	0.334	14.087	0.090	0.813
URetinexNet	10.903	0.600	0.402	10.894	0.610	0.356	15.519	0.323	0.599
RUAS	8.684	0.493	0.525	8.628	0.494	0.499	12.622	0.081	0.920
LLFlow	12.737	0.617	0.388	12.737	0.617	0.388	16.226	0.367	0.619
LEDNet	12.668	0.579	0.412	12.551	0.576	0.383	20.830	0.648	0.471
<b>CIDNet</b>	<b>13.425</b>	<b>0.636</b>	<b>0.362</b>	<b>13.446</b>	<b>0.648</b>	<b>0.318</b>	<b>22.904</b>	<b>0.676</b>	<b>0.411</b>

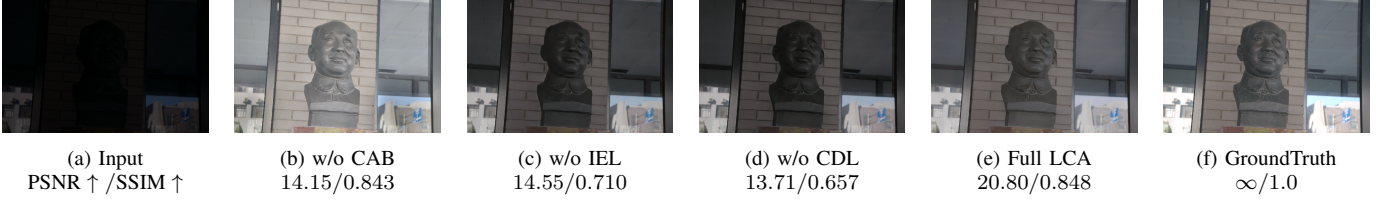


Fig. 8: The visual quality comparison results on LOLv2-Real dataset with various LCA blocks (by removing submodules in the LCA). (e) Full LCA denotes the original design of the LCA block.

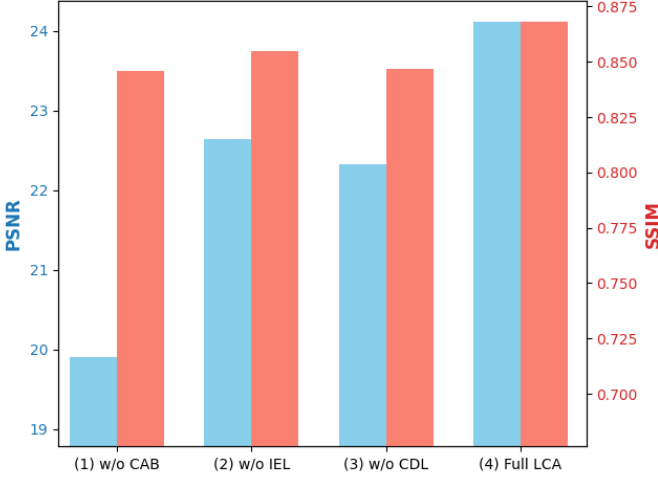


Fig. 9: Ablation experiment of the submodules CAB, IEL, and CDL in LCA. The impact of CAB is significantly higher than the other two modules, indicating that our designed cross-attention can better enhance the image to the appropriate brightness level. (Full LCA denotes the origin design of the LCA block.)

previous SOTA methods. Notably, our method exhibits a substantial improvement in the NIQE metric compared to other approaches.

For each of these five unpaired datasets, we randomly selected an image in each dataset and compared it visually. As Fig. 7, CIDNet improves the brightness and increases the perceived level of the image while ensuring reasonable color accuracy compared with RUAS, ZeroDCE, RetinexNet, KinD and PairLIE.

### C. Ablation Study

We conduct extensive ablation studies to validate our HVI color space and several modules. The evaluations are all performed on the LOLv2-Real dataset for fast convergence and stable performance.

**Color Spaces.** We conduct an ablation on sRGB, HSV and our HVI on CIDNet as Table V. The ranking of image restoration quality with CIDNet is as follows: HVI, sRGB, and HSV. Comparing row (2), (3), and (6), the best is HVI color space, which exists a significant performance enhancement.

**Structures and Modules.** First, we examine our LCA module in the present color spaces. As shown in Table V row (1), (2), and (6), LCA with baseline gains 2.088, 5.428 dB on PSNR for sRGB and HVI respectively. Second, in our experimental investigation, we have observed distinct statistical

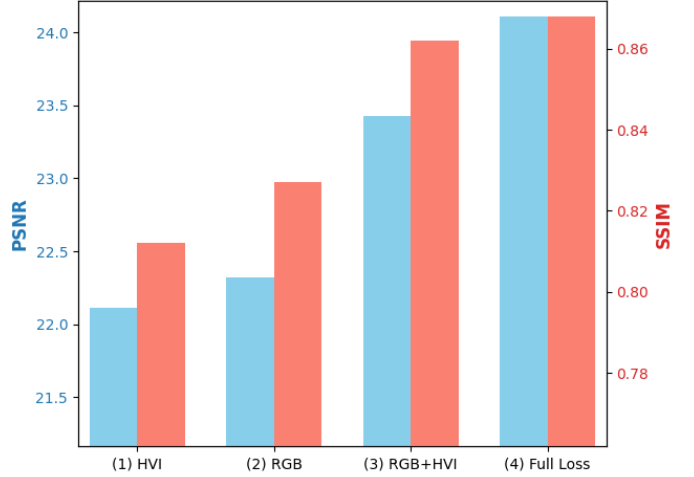


Fig. 10: Ablation of losses in our HVI color space, the sRGB color space, and the potential feature space as the perceptual (Perc.) loss with VGG19 network [36]. In the group (4), we incorporate the perceptual loss into both the HVI and sRGB color spaces simultaneously.

patterns between the I-branch and HV-branch. As shown in Table V row (6) and (7), dividing the Enhancement Network into dual branches enhances 1.159 dB in PSNR. Third, by decoupling the image through HVI, a certain correlation between the values of the I-map and the noise of the HV-map can be discovered. To establish the relationship mapping, we incorporate Cross-Attention into the internal of LCA. As Table V row (8), PSNR and SSIM are both greater than row (7) by 0.952 dB and 0.014. Last, as Fig. 9, removing the CAB, CDL or IEL clearly shows a decrease effect of PSNR and SSIM, which demonstrates the effectiveness of sub-modules in LCA block. The visual quality comparisons are shown in Fig. 8. Specifically, removing CAB leads to unstable brightness enhancement, resulting in local overexposure and artifacts. On the other hand, removing IEL or CDL results in excessively dark brightness, thereby affecting the details.

**Ablation on loss function.** We conduct an ablation by progressively adding loss on (1)HVI-map, (2)sRGB-image, (3)HVI and sRGB, (4)Perceptual loss on both color space as Table 10. Compared to the previous groups, the results of including the loss in all spaces in group (4) shows an improvement in PSNR of 1.998 dB, 1.792 dB, and 0.684 dB. This demonstrates the effectiveness of the loss function we designed.

**Analysis.** Above experiments sequentially verify the supe-

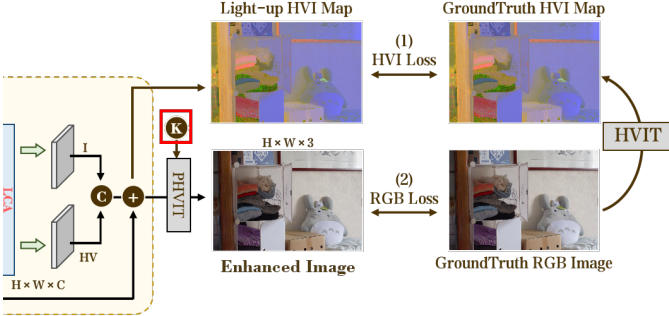


Fig. 11: Comparison of loss function computation positions. The trainable parameter  $k$  is highlighted within the red box. (Zoom in for the best view.)

riority of our the HVI color space, the LCA block, and the dual-branch Enhancement Network with Cross-Attention. For loss ablation experiment, the HVI color space needs to be supervised by the sRGB space losses in order to perform.

**Loss Discussion: Why is HVI loss performance weaker than RGB loss?** In Table 10, the results in group (2) outperform those in the first group. The reason is that the loss functions of HVI and RGB operate at different positions in our network. As presented in Fig. 11, in between the losses of HVI and RGB lies the inverse transformation of HVI, which incorporates a trainable parameter  $k$ . Using only the HVI loss does not allow  $k$  to converge to the optimal solution and the loss in RGB color space is needed to assist in the training process. Therefore, the combination of HVI and RGB losses has achieved better performance as shown in the third group of Fig. 10.

#### D. Robustness Experiments

**LOL-Blur.** Long exposures in dimly lit environments can result in photos that are prone to blurring. To verify the robustness ability of our model, we conduct experiments on the low-light blur dataset LOL-Blur.

TABLE VI: Quantitative evaluation on LOL-Blur dataset. PSNR↑ and SSIM↑: the higher, the better; LPIPS↓ and FLOPs↓: the lower, the better. The symbol ‘†’ indicates that we use DeblurGAN-v2 trained on RealBlur [50] dataset. ‘‡’ indicates the network is retrained on the LOL-Blur dataset. The highest result is in red color.

Methods	PSNR↑	SSIM↑	LPIPS↓	FLOPs↓
ZeroDCE [4] → MIMO [51]	17.680	0.542	0.422	-
DeblurGAN <sup>†</sup> [52] → ZeroDCE [4]	18.330	0.589	0.384	-
RetinexFormer <sup>‡</sup> [14]	22.904	0.824	0.236	15.85
MIMO <sup>†</sup> [51]	24.410	0.835	0.183	62.36
LEDNet <sup>‡</sup> [35]	25.271	0.859	0.141	35.93
<b>CIDNet<sup>‡</sup></b>	<b>26.572</b>	<b>0.890</b>	<b>0.120</b>	<b>7.57</b>

TABLE VII: Robustness testing experiments. All methods is trained on the LOLv1 and tested in the LOLv2-Syn dataset. The best result is in red color.

Methods	LLFlow	RUAS	PairLIE	RetinexFormer	LEDNet	<b>CIDNet</b>
PSNR↑	17.1191	15.3257	<b>19.0743</b>	16.1834	16.6210	18.6382
SSIM↑	0.8117	0.4883	0.7965	0.7693	0.7733	<b>0.8200</b>
LPIPS↓	0.2239	0.4577	0.2300	0.2515	0.2196	<b>0.2154</b>



Fig. 12: Visual comparison on LOL-Blur dataset. Compared to other methods, our CIDNet is closer to GroundTruth and more dominant in visual recognition. (Zoom in for best view.)

In the first set, we perform lighting-up with ZeroDCE and then deblurring with MIMO [51]. In the second set, we perform deblurring with DeblurGAN-v2 [52] and then light up with ZeroDCE. In the third group, we have retrained on LOL-Blur with four methods, RetinexFormer, MIMO, and LEDNet, and compared them with our CIDNet. The results (as Table VI) show that the quantitative comparison of CIDNet against the current stage SOTA method LEDNet by 5.15%, 3.61%, and 14.89% in PSNR, SSIM, and LPIPS metrics respectively. Not only that, the FLOPs of our model are the lowest among these methods.

As shown in Fig. 12, we have taken a set of blurred images, recovered them using different methods, and compared them with GroundTruth. The experimental results reveal that the image reconstructions achieved by CIDNet exhibit a notable improvement in visual comfort and perceptual recognition, thereby enhancing the overall quality and interpretability of the generated images.

**Cross dataset validation.** To verify the generalization ability of our model, we take the model trained on LOLv1 [6] and tested it on LOLv2-Syn [27] as Table VII. Compared with three supervised learning SOTA models, LLFlow [5], RetinexFormer [14], and LEDNet [35], our model comprehensively outperforms in three metrics. And compared with the unsupervised models PairLIE [7] and RUAS [39], which have better generalization ability, our CIDNet also completely outperforms SSIM and LPIPS.

**The effect of HVIT in other methods.** We employ the HVI transform as a versatile module to examine the resilience of our HVI space across multiple models. To this end, the HVIT and PHVIT are incorporated into four supervised models, RetinexFormer, LEDNet, Restormer, and SNR-Aware. Subsequently, these models are retrained and evaluated on the LOLv2-Real [27] dataset. The outcomes, as illustrated in Table VIII, demonstrate the remarkable enhancement achieved by our HVI space in the performance of each method. Impressively, all eleven metrics associated with the four methods exhibit substantial improvements. Moreover, the proposed CIDNet demonstrates superior performance not only in terms of PSNR and SSIM, but also exhibits the shortest CPU (AMD Ryzen 9 5900HX) and GPU (NVIDIA 2080Ti) inference time and minimal computational (FLOPs) overhead.

TABLE VIII: HVI transform robustness validation experiments. Embedding HVI transform into other methods and training/testing on LOLv2-Real. Value in brackets represents the amount of better numerical changes with red color. The best result of PSNR/SSIM $\uparrow$  and LPIPS/FLOPs $\downarrow$  is in **bolded**. The lowest time of inference with  $256 \times 256$  in three channels is also in **bolded**.

Methods	RetinexFormer	LEDNet	Restormer	SNR-Aware	CIDNet
PSNR $\uparrow$	23.600( <b>+0.806</b> )	23.394( <b>+3.456</b> )	23.234( <b>+4.541</b> )	22.251( <b>+0.771</b> )	<b>24.111</b>
SSIM $\uparrow$	0.865( <b>+0.025</b> )	0.837( <b>+0.010</b> )	0.866( <b>+0.032</b> )	0.840(0.009)	<b>0.868</b>
LPIPS $\downarrow$	0.113( <b>-0.058</b> )	0.117( <b>-0.003</b> )	<b>0.093(-0.022)</b>	0.117( <b>-0.040</b> )	0.108
FLOPs/G $\downarrow$	15.85	35.92	114.25	26.35	<b>7.57</b>
GPU Time/s $\downarrow$	0.062	0.070	0.183	0.054	<b>0.053</b>
CPU Time/s $\downarrow$	0.594	0.846	5.898	1.751	<b>0.416</b>

TABLE IX: Ablation of three different types of inputs in Enhancement Network. Each distinct convolution layers will extract and generate corresponding intensity features (as I-Feature) and HV-features from different input maps (the type of input is indicated in the columns I-Feature and HV-Feature). The best result is in red color.

Types	I-Features	HV-Features	PSNR $\uparrow$	SSIM $\uparrow$	LPIPS $\downarrow$
(1) Half-HVIT	intensity	HVI-Map	<b>24.111</b>	<b>0.868</b>	<b>0.108</b>
(2) Separate-HVIT	intensity	HV-Map	23.734	0.857	0.141
(3) Full-HVIT	HVI-Map	HVI-Map	23.814	0.859	0.127

### E. Variant HVIT Experiments and Discussion

To investigate how the first two  $3 \times 3$  convolution layers (in Enhancement Network) learned to generate I-feature and HV-feature, we further develop three different HVIT by changing the inputs. As shown in Table IX row (1), the Half-HVIT utilized in our pipeline generates intensity features (hereinafter abbreviated as I-Features) from the intensity Map and HV-Features from the HVI-Map. We have respectively modified the input of I-Features and HV-Features, leading to the creation of two new HVIT models in Table IX row (2) and row (3). The Separate-HVIT replaces the input of HV-Feature with HV-Map, while the Full-HVIT substitutes the input of I-Feature with HVI-Map.

As a result, the Half-HVIT achieves the best restoration results among the three HVIT models. The performance drop of the Separate-HVIT is more pronounced, with reductions of 0.377 dB in PSNR, 0.011 in SSIM, and 0.033 in LPIPS. This can be attributed to the lower information content in the HV features compared to the HVI-Map, which lacks guidance from the intensity part. On the other hand, the performance decline of the Full-HVIT was due to the interference noise information in the HVI-Map for extracting I-Features, leading to convolutional layers failing to accurately extract key features.

## VI. CONCLUSION

In this paper, we present a novel method for low-light image enhancement using the proposed HVI color space with trainable parameters and the CIDNet to decouple image brightness and color and adapt to various illumination scales. The dual-branch network, build upon the HVI color space, simultaneously processes brightness and color, aided by the plug-and-play LCA module and symmetric HVI Transform module. Our CIDNet outperforms all types of SOTA methods across 11 datasets with lower FLOPs and parameters.

## ACKNOWLEDGMENT

This work is supported by NSFC of China 62301432, 6230624, Natural Science Basic Research Program of Shaanxi No. 2023-JC-QN-0685, QCYRCXM-2023-057, the Fundamental Research Funds for the Central Universities No. D5000220444.

## REFERENCES

- [1] C. Li, C. Guo, L. Han, J. Jiang, M.-M. Cheng, J. Gu, and C. C. Loy, “Low-light image and video enhancement using deep learning: A survey,” *IEEE Transactions on Pattern Analysis and Machine Intelligence*, vol. 44, no. 12, pp. 9396–9416, 2022.
- [2] Y. Zhang, J. Zhang, and X. Guo, “Kindling the darkness: A practical low-light image enhancer,” in *Proceedings of the 27th ACM International Conference on Multimedia*, ser. MM ’19. New York, NY, USA: ACM, 2019, pp. 1632–1640. [Online]. Available: <http://doi.acm.org/10.1145/3343031.3350926>
- [3] Y. Jiang, X. Gong, D. Liu, Y. Cheng, C. Fang, X. Shen, J. Yang, P. Zhou, and Z. Wang, “Enlightengan: Deep light enhancement without paired supervision,” *IEEE Transactions on Image Processing*, vol. 30, pp. 2340–2349, 2021.
- [4] C. G. Guo, C. Li, J. Guo, C. C. Loy, J. Hou, S. Kwong, and R. Cong, “Zero-reference deep curve estimation for low-light image enhancement,” in *Proceedings of the IEEE conference on computer vision and pattern recognition (CVPR)*, June 2020, pp. 1780–1789.
- [5] Y. Wang, R. Wan, W. Yang, H. Li, L.-P. Chau, and A. C. Kot, “Low-light image enhancement with normalizing flow,” *arXiv preprint arXiv:2109.05923*, 2021.
- [6] C. Wei, W. Wang, W. Yang, and J. Liu, “Deep retinex decomposition for low-light enhancement,” 2018.
- [7] Z. Fu, Y. Yang, X. Tu, Y. Huang, X. Ding, and K.-K. Ma, “Learning a simple low-light image enhancer from paired low-light instances,” in *Proceedings of the IEEE/CVF Conference on Computer Vision and Pattern Recognition*, 2023, pp. 22 252–22 261.
- [8] X. Guo and Q. Hu, “Low-light image enhancement via breaking down the darkness,” *International Journal of Computer Vision*, vol. 131, no. 1, pp. 48–66, Jan 2023. [Online]. Available: <https://doi.org/10.1007/s11263-022-01667-9>
- [9] M. Abdullah-Al-Wadud, M. H. Kabir, M. A. A. Dewan, and O. Chae, “A dynamic histogram equalization for image contrast enhancement,” in *2007 Digest of Technical Papers International Conference on Consumer Electronics*, 2007, pp. 1–2.
- [10] S.-C. Huang, F.-C. Cheng, and Y.-S. Chiu, “Efficient contrast enhancement using adaptive gamma correction with weighting distribution,” *IEEE Transactions on Image Processing*, vol. 22, no. 3, pp. 1032–1041, 2013.
- [11] X. Fu, D. Zeng, Y. Huang, X.-P. Zhang, and X. Ding, “A weighted variational model for simultaneous reflectance and illumination estimation,” in *2016 IEEE Conference on Computer Vision and Pattern Recognition (CVPR)*, 2016, pp. 2782–2790.
- [12] X. Guo, Y. Li, and H. Ling, “Lime: Low-light image enhancement via illumination map estimation,” *IEEE Transactions on Image Processing*, vol. 26, no. 2, pp. 982–993, 2017.
- [13] K. G. Lore, A. Akintayo, and S. Sarkar, “Llnet: A deep autoencoder approach to natural low-light image enhancement,” 2016.
- [14] Y. Cai, H. Bian, J. Lin, H. Wang, R. Timofte, and Y. Zhang, “Retinex-former: One-stage retinex-based transformer for low-light image enhancement,” in *Proceedings of the IEEE/CVF International Conference on Computer Vision (ICCV)*, October 2023, pp. 12 504–12 513.
- [15] X. Xu, R. Wang, C.-W. Fu, and J. Jia, “Snr-aware low-light image enhancement,” in *2022 IEEE/CVF Conference on Computer Vision and Pattern Recognition (CVPR)*, 2022, pp. 17 693–17 703.
- [16] J. Ho, A. Jain, and P. Abbeel, “Denoising diffusion probabilistic models,” in *Advances in Neural Information Processing Systems*, H. Larochelle, M. Ranzato, R. Hadsell, M. Balcan, and H. Lin, Eds., vol. 33. Curran Associates, Inc., 2020, pp. 6840–6851.
- [17] D. Zhou, Z. Yang, and Y. Yang, “Pyramid diffusion models for low-light image enhancement,” *arXiv preprint arXiv:2305.10028*, 2023.
- [18] Y. Wu, G. Wang, Z. Wang, Y. Yang, T. Li, P. Wang, C. Li, and H. T. Shen, “Reco-diff: Explore retinex-based condition strategy in diffusion model for low-light image enhancement,” *arXiv preprint arXiv:2312.12826*, 2023.

- [19] J. Hou, Z. Zhu, J. Hou, H. Liu, H. Zeng, and H. Yuan, "Global structure-aware diffusion process for low-light image enhancement," *Advances in Neural Information Processing Systems*, vol. 36, 2024.
- [20] X. Yi, H. Xu, H. Zhang, L. Tang, and J. Ma, "Diff-retinex: Rethinking low-light image enhancement with a generative diffusion model," in *Proceedings of the IEEE/CVF International Conference on Computer Vision*, 2023, pp. 12 302–12 311.
- [21] C. Poynton, "18 - image digitization and reconstruction," in *Digital Video and HDTV*, ser. The Morgan Kaufmann Series in Computer Graphics, C. Poynton, Ed. San Francisco: Morgan Kaufmann, 2003, pp. 187–194. [Online]. Available: <https://www.sciencedirect.com/science/article/pii/B9781558607927500847>
- [22] J. D. Foley and A. van Dam, "Fundamentals of interactive computer graphics," 1982. [Online]. Available: <https://api.semanticscholar.org/CorpusID:62562590>
- [23] A. Brateanu, R. Balmez, A. Avram, and C. Orhei, "Lyt-net: Lightweight yuv transformer-based network for low-light image enhancement," 2024.
- [24] A. Dosovitskiy, L. Beyer, A. Kolesnikov, D. Weissenborn, X. Zhai, T. Unterthiner, M. Dehghani, M. Minderer, G. Heigold, S. Gelly, J. Uszkoreit, and N. Houlsby, "An image is worth 16x16 words: Transformers for image recognition at scale," 2021.
- [25] G. Seif and D. Androultsos, "Edge-based loss function for single image super-resolution," in *2018 IEEE International Conference on Acoustics, Speech and Signal Processing (ICASSP)*, 2018, pp. 1468–1472.
- [26] J. Johnson, A. Alahi, and L. Fei-Fei, "Perceptual losses for real-time style transfer and super-resolution," 2016.
- [27] W. Yang, W. Wang, H. Huang, S. Wang, and J. Liu, "Sparse gradient regularized deep retinex network for robust low-light image enhancement," vol. 30, 2021, pp. 2072–2086.
- [28] C. Lee, C. Lee, and C.-S. Kim, "Contrast enhancement based on layered difference representation of 2d histograms," *IEEE Transactions on Image Processing*, vol. 22, no. 12, pp. 5372–5384, 2013.
- [29] K. Ma, K. Zeng, and Z. Wang, "Perceptual quality assessment for multi-exposure image fusion," *IEEE Transactions on Image Processing*, vol. 24, no. 11, pp. 3345–3356, 2015.
- [30] S. Wang, J. Zheng, H.-M. Hu, and B. Li, "Naturalness preserved enhancement algorithm for non-uniform illumination images," *IEEE transactions on image processing : a publication of the IEEE Signal Processing Society*, vol. 22, 05 2013.
- [31] V. Vonikakis, R. Kouskouridas, and A. Gasteratos, "On the evaluation of illumination compensation algorithms," *Multimedia Tools and Applications*, vol. 77, pp. 1–21, 04 2018.
- [32] J. Cai, S. Gu, and L. Zhang, "Learning a deep single image contrast enhancer from multi-exposure images," *IEEE Transactions on Image Processing*, vol. 27, no. 4, pp. 2049–2062, 2018.
- [33] S. Zheng, Y. Ma, J. Pan, C. Lu, and G. Gupta, "Low-light image and video enhancement: A comprehensive survey and beyond," *arXiv preprint arXiv:2212.10772*, 2022.
- [34] C. Chen, Q. Chen, J. Xu, and V. Koltun, "Learning to see in the dark," in *CVPR*, 2018.
- [35] S. Zhou, C. Li, and C. C. Loy, "Lednet: Joint low-light enhancement and deblurring in the dark," in *ECCV*, 2022.
- [36] K. Simonyan and A. Zisserman, "Very deep convolutional networks for large-scale image recognition," in *International Conference on Learning Representations*, 2015.
- [37] H. Zeng, J. Cai, L. Li, Z. Cao, and L. Zhang, "Learning image-adaptive 3d lookup tables for high performance photo enhancement in real-time," *IEEE Transactions on Pattern Analysis and Machine Intelligence*, vol. 44, no. 04, pp. 2058–2073, 2020.
- [38] W. Yang, S. Wang, Y. Fang, Y. Wang, and J. Liu, "From fidelity to perceptual quality: A semi-supervised approach for low-light image enhancement," in *IEEE/CVF Conference on Computer Vision and Pattern Recognition (CVPR)*, June 2020.
- [39] L. Risheng, M. Long, Z. Jiaao, F. Xin, and L. Zhongxuan, "Retinex-inspired unrolling with cooperative prior architecture search for low-light image enhancement," in *Proceedings of the IEEE Conference on Computer Vision and Pattern Recognition*, 2021.
- [40] S. W. Zamir, A. Arora, S. Khan, M. Hayat, F. S. Khan, and M.-H. Yang, "Restormer: Efficient transformer for high-resolution image restoration," in *CVPR*, 2022.
- [41] T. Wang, K. Zhang, T. Shen, W. Luo, B. Stenger, and T. Lu, "Ultra-high-definition low-light image enhancement: A benchmark and transformer-based method," in *Proceedings of the AAAI Conference on Artificial Intelligence*, vol. 37, no. 3, 2023, pp. 2654–2662.
- [42] D. P. Kingma and J. Ba, "Adam: A method for stochastic optimization," 2017.
- [43] I. Loshchilov and F. Hutter, "Sgdr: Stochastic gradient descent with warm restarts," 2017.
- [44] Z. Wang, A. Bovik, H. Sheikh, and E. Simoncelli, "Image quality assessment: from error visibility to structural similarity," *IEEE Transactions on Image Processing*, vol. 13, no. 4, pp. 600–612, 2004.
- [45] R. Zhang, P. Isola, A. A. Efros, E. Shechtman, and O. Wang, "The unreasonable effectiveness of deep features as a perceptual metric," in *CVPR*, 2018.
- [46] A. Krizhevsky, I. Sutskever, and G. Hinton, "Imagenet classification with deep convolutional neural networks," *Advances in neural information processing systems*, vol. 25, no. 2, 2012.
- [47] A. Mittal, A. K. Moorthy, and A. C. Bovik, "No-reference image quality assessment in the spatial domain," *IEEE Transactions on Image Processing*, vol. 21, no. 12, pp. 4695–4708, 2012.
- [48] A. Mittal, R. Soundararajan, and A. C. Bovik, "Making a "completely blind" image quality analyzer," *IEEE Signal Processing Letters*, vol. 20, no. 3, pp. 209–212, 2013.
- [49] O. Petit, N. Thome, C. Rambour, and L. Soler, "U-net transformer: Self and cross attention for medical image segmentation," 2021.
- [50] J. Rim, H. Lee, J. Won, and S. Cho, "Real-world blur dataset for learning and benchmarking deblurring algorithms," in *Proceedings of the European Conference on Computer Vision (ECCV)*, 2020.
- [51] S.-J. Cho, S.-W. Ji, J.-P. Hong, S.-W. Jung, and S.-J. Ko, "Rethinking coarse-to-fine approach in single image deblurring," 2021.
- [52] O. Kupyn, T. Martyniuk, J. Wu, and Z. Wang, "Deblurgan-v2: Deblurring (orders-of-magnitude) faster and better," in *The IEEE International Conference on Computer Vision (ICCV)*, Oct 2019.